Photovoltaic cells

DOI: 10.1002/smll.200701309

# Nanowelded Carbon-Nanotube-Based Solar Microcells**

*Changxin Chen,* Yang Lu, Eric S. Kong, Yafei Zhang,* and Shuit-Tong Lee*

Photovoltaic (PV) cells are of immense interest due to their vast application potential in the fields of energy and communication.[1–3] The adoption of ideal photoactive material and the design of optimum device structure are critical to achieving low-cost, high-efficiency PV cells. The semiconducting single-walled carbon nanotubes (SWNTs) are potentially an attractive material for PV applications due to their many unique structural and electrical properties. They are almost defect free to greatly decrease carrier recombination, bear a wide range of direct bandgaps matching the solar spectrum,[4–6] and show strong photoabsorption[7–10] and photoresponse[11–15] from ultraviolet to infrared, and exhibit high carrier mobility [16] and reduced carrier transport scattering.[17,18] Indeed, previous studies had attempted to fabricate SWNT films into photoelectrochemical solar cells.[19] However, due to the inefficient separation and collection of photoexcited carriers and large intertube interaction, the maximum monochromatic incident photo-to-current conversion efficiency (IPCE) obtained for the cell is only 0.15%. Here, we report a novel approach that enables fabricating SWNT PV solar microcells with high power-conversion efficiency. In this cell, a directed array of monolayer SWNTs was nanowelded onto two asymmetrical metal electrodes with high and low work functions, respectively, resulting in a strong built-in electric field in SWNTs for efficient separation of photogenerated electron–hole pairs. Under solar illumination, the monolayer SWNT PV cell shows a power conversion efficiency of 0.80% and 0.31% at an illumination intensity of 8.8 W $cm^{-2}$ and 100 mW $cm^{-2}$, respectively. Correspondingly, a remarkable efficiency of 12.6% and 5.1% was estimated based on the actual absorbed incident power. Our results demonstrate the exciting application potential of SWNTs for PV devices.

A schematic diagram of our SWNT PV cell is shown in Figure 1a. In the experiment, Pd and Al metals, with a high and a low work function ($\Phi$) of 5.1 eV and 4.1 eV, respectively,[20] were chosen as the drain and source contact electrodes. Using standard UV lithography and lift-off process, the two metals were patterned by the overlay on silicon wafers with a 500-nm thermally oxidized layer, forming the parallel electrode pairs. The electrodes were 150 nm in thickness, 40 μm in width, 50 μm in length, and separated by 500 nm. A 200-nm-thick Al electrode was sputtered on the back of Si substrate, through which a gate voltage was supplied to the Si substrate for modulating the SWNT–metal contact barrier. The SWNTs synthesized by the catalytic chemical vapor deposition (CVD) method with an average diameter of 0.9 nm ($\Phi \approx 4.5$ eV, $E_g \approx 1.1$ eV[21]) were dispersed fully in chloroform and aligned onto the source and drain electrodes by an AC dielectrophoresis method to form the dispersed parallel SWNT bundle array.[22] Then, an ultrasonic nanowelding technique was applied to bond the SWNTs onto the metal electrodes.[23,24] The SWNTs were pressed against the electrodes by a welding head of $Al_2O_3$ crystal vibrating at ultrasonic frequency, causing the SWNTs welded into the electrodes to form the firm and low-resistance contacts. Figure 1b shows the scanning electron microscopy (SEM) image of the SWNT bundle array bridging the electrodes after the ultrasonic nanowelding. The two ends of the SWNT bundles are almost invisible on the electrodes as a result of being welded into the electrodes, as shown in Figure 1c. At this point, a stepwise-increased negative drain bias was applied in the devices in order to produce a large enough current to selectively burn off the metallic SWNTs in the array,[25] while the semiconducting SWNTs were protected in this process because only a very small reverse-biased current flows through them. Finally, the devices were capped with a 10-nm CVD $SiO_2$ film to exclude effects such as the photodesorption of oxygen during illumination, which could alter the band lineup at the Schottky contact barriers.[26,27] The optical measurements of the as-prepared devices were carried out under a different intensity of solar-simulated light (AM1.5 G) illumination, with the incidence direction vertical to the plane of the SWNT bundle array. The back-gate bias was kept at zero voltage during the test. Agilent 4156C semiconductor parameter analyzer was used to drive the devices as well as to monitor the current through the devices.

Figure 2 shows the typical dark current–voltage ($I$–$V$) characteristics of SWNT PV cells with 146 SWNT bundles bridging the electrodes. In the dark, the devices show rectifying $I$–$V$ characteristics (inset of Figure 2). This can be attributed to the formation of Schottky barriers at metal–nanotube contacts.[28–30] Previous studies suggested that the Fermi level of Pd would be located at or even slightly lower than the top of the valence band of SWNTs at the Pd–SWNT

[*] Dr. C. Chen, Y. Lu, Prof. E. S. Kong, Prof. Y. Zhang
National Key Laboratory of Nano/Micro Fabrication Technology
Key Laboratory for Thin Film and Microfabrication of the Ministry of Education
Institute of Micro/Nano Science and Technology
Shanghai Jiao Tong University
Shanghai 200240 (P.R. China)
E-mail: chen.c.x@sjtu.edu.cn; yfzhang@sjtu.edu.cn
Prof. S. T. Lee
Center of Super-Diamond and Advanced Films (COSDAF) and Department of Physics and Materials Science
City University of Hong Kong, Hong Kong SAR
Nano-Organic Photoelectronic Laboratory
Technical Institute of Physics and Chemistry
Chinese Academy of Science
Beijing 100101 (P.R. China)

[**] This work is supported by Shanghai Science and Technology Grant No. 0752nm015, National Natural Science Foundation of China No. 50730008, and National Basic Research Program of China No.2006CB300406. The Instrumental Analysis Center of Shanghai Jiao Tong University is acknowledged for testing support.

Supporting Information is available on the WWW under http://www.small-journal.com or from the author.

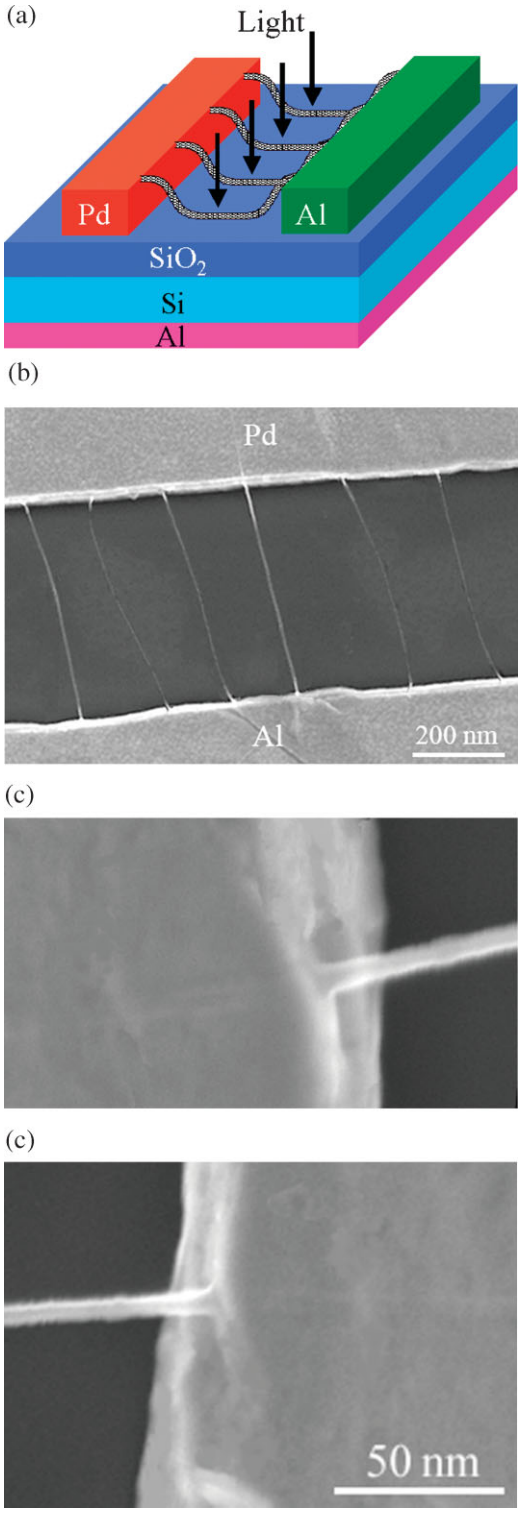


**Figure 1.** Structure of the SWNT PV microcells based on nanowelded metal(A)/nanotube/metal(B) junctions. a) Schematic diagram of SWNT PV cells. b) SEM image of SWNT bundle array bridging the Pd and Al electrodes. c) SEM images of the SWNT bundle ends nanowelded onto the metal electrodes.

contact,[31,20] and the Fermi level of Al would be close to the bottom of the conduction band of SWNTs at the Al–SWNT contact.[20] Due to the fact that the Fermi levels of Pd and Al are below and above the Fermi level of SWNTs, respectively,

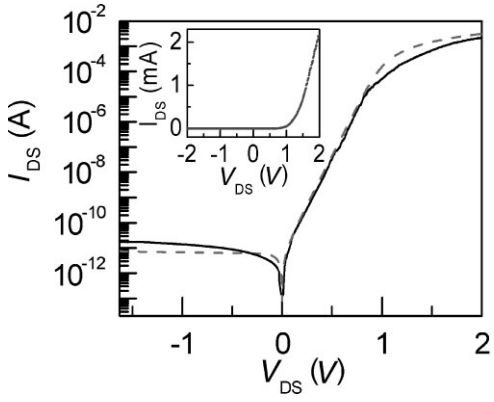


**Figure 2.** Logarithmic plot of dark *I–V* characteristics of the SWNT PV cell with 146 SWNT bundles bridging the electrodes at $T = 300$ K. The dashed line shows a fit of Equation (4) using $I_S = 5$ pA, $n = 1.9$ and $R_S = 271\ \Omega$. Inset: linear plot of *I–V* characteristics.

the p- and n-type Schottky barriers are accordingly formed at the two contacts when no gate voltage is applied. Therefore, the physical structure of the device is analogous to a p–i–n junction diode, exhibiting the rectifying *I–V* characteristics. By fitting the dark *I–V* curves with the diode Equation (4) (see below), we deduced that a small reverse saturation current (or the leakage current) on the order of $I_S \approx 5$ pA was

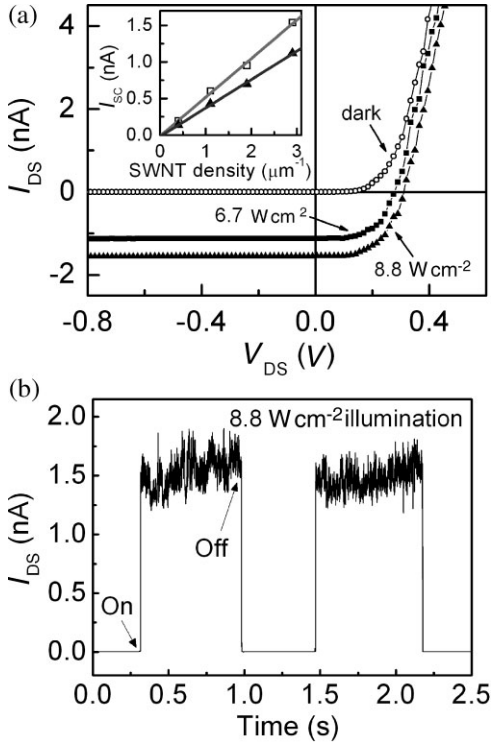


**Figure 3.** Illumination characteristics of the SWNT PV cell with 146 SWNTs bridging the electrodes. a) *I–V* characteristics measured in the dark and under illumination at $V_G = 0$, showing the PV effect of the devices. The inset displays the dependency of $I_{SC}$ on SWNT density (=SWNT number/electrode length) in the devices; the lines fitted to the hollow square and solid triangle represent the data obtained at illumination intensity of 6.7 W cm$^{-2}$ and 8.8 W cm$^{-2}$, respectively. b) The time-resolved trace of the current in the device with the light chopped, taken with zero drain bias and a gate voltage of $V_G = 0$.

achieved in our devices with an ideality factor $n$ ranging from 1.4 to 1.9 (see Figure 2).

When illuminated by light, the devices showed PV effects and photocurrent at zero voltage bias ($I_{SC}$; see Figure 3a). Under a forward bias, the photocurrent is opposite to the forward-biased current of the device. At $V_{DS} = V_{OC}$ (open-circuit voltage), these two currents cancel and result in a zero net current. As shown in Figure 3a, when the illumination power density of 6.7 W cm$^{-2}$ was applied, the $I_{SC}$ and $V_{OC}$ were 1.12 nA and 0.28 V, respectively. With power density increased to 8.8 W cm$^{-2}$, the $I_{SC}$ and $V_{OC}$ increased to 1.54 nA and 0.31V, respectively. The PV effect could be attributed to a strong electric field along the nanotube derived from the asymmetric contacts, which efficiently separates the photogenerated electron–hole pairs. Although previous studies have shown that the asymmetric geometrical arrangement of the nanotubes in the devices could also cause a small photovoltage,[12] this origin can be ruled out in our devices since only a very weak photovoltage was observed at $V_G = 0$ when the same source and drain electrodes were used.[12] To check the effect of SWNT density on the PV effect, different densities (up to 2.9 μm$^{-1}$) of SWNT bundle arrays were investigated. It was found that the $I_{SC}$ had an approximately linear dependency on SWNT density in the measured region (as shown in the inset of Figure 3a), whereas no apparent dependency was observed between the $V_{OC}$ and SWNT density. Figure 3b shows the time trace of the photocurrent in the devices at zero drain bias when chopping the incident light. It shows that the photocurrent was induced instantly as the incident light was turned on with a response time of about 90 ms. The short response time demonstrates that this current derives from the movement of light-excited carriers in SWNTs.[11]

The essential physics of operation of the SWNT PV cell is illustrated in the energy band diagram of the initial equilibrium state (Figure 4a). The difference in the values of the work functions of the source and drain electrodes causes the bending of the energy bands in SWNTs. At the two ends of SWNTs, two Schottky barriers are formed at metal–nanotube contacts in an equilibrium state. Due to the fact that the gate oxide thickness is on the order of (equal to) the SWNT channel length in our devices, the band bending for the SWNT would extend into the middle of the device because of the weak coupling of the gate to the channel.[12,32,33] Early studies have indicated that the band bending could extend to a distance of micrometers or more when lightly doped SWNTs are connected to the metal.[33] Thus, a strong built-in electric field covering the whole SWNT channel would form to separate the carriers, which is ideal for high-efficiency carrier separation. Under illumination, the photogenerated electron–hole pairs in the device are separated by the built-in electric field to flow toward the two ends of SWNTs and ultimately collected at the source and drain electrodes, inducing the photovoltage. Although early bulk semiconductor devices also utilized metal–semiconductor Schottky contacts to fabricate PV cells, the devices were inefficient due to the fact that the full bandgap of the semiconductor is never utilized as a result of interface states and Fermi-level pinning,[34] which cause reduced photovoltage and high leakage currents. The SWNTs have a unique one-dimensional (1D) structure with fully

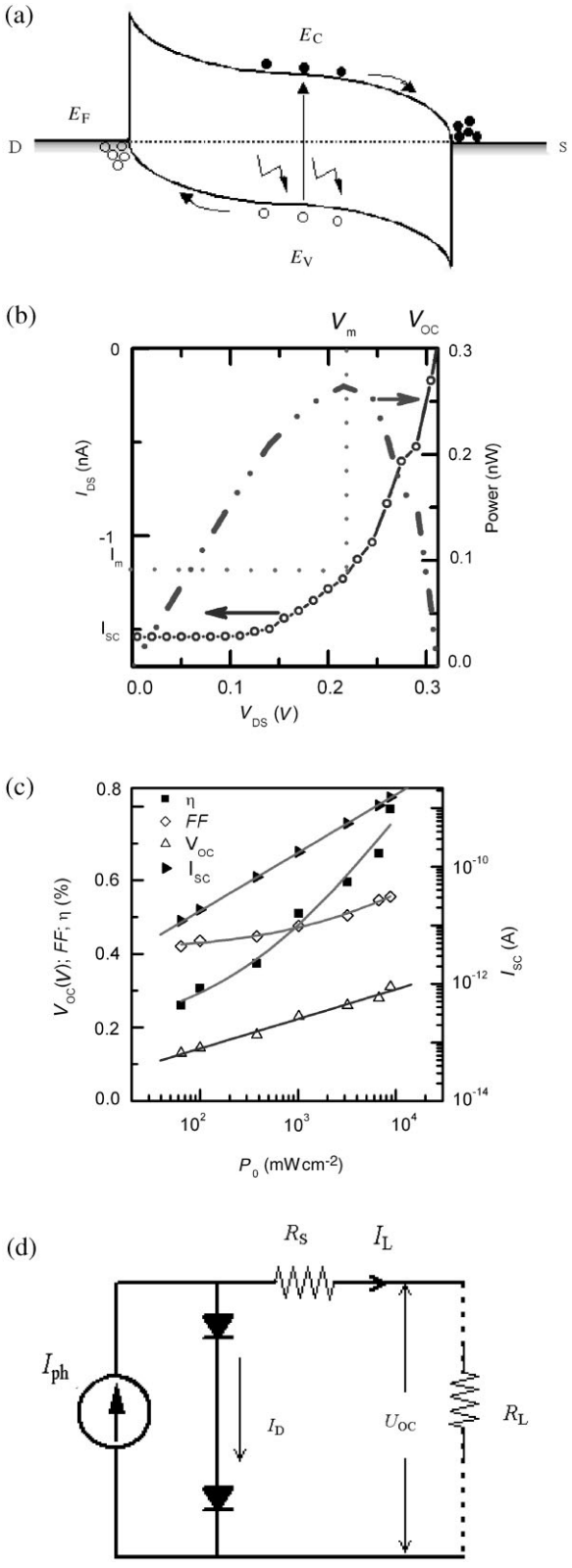


**Figure 4.** Analysis of the mechanism and performances for the SWNT PV cells. a) The energy-band diagram of SWNTs bridging two dissimilar metal electrodes, showing the currents from photogenerated electron–hole pairs. b) The fourth-quadrant $I$–$V$ curve and corresponding power generation (power = $I_{DS} \times V_{DS}$) at an illumination intensity of 8.8 W cm$^{-2}$. c) Key cell-performance parameters as a function of the incident power density. d) The equivalent circuit of the cells.

saturated surface bonds and no interface states. Therefore, no Fermi-level pinning exists at the metal–nanotube contacts.[20] Thus, it is possible to utilize the full bandgap of SWNTs by choosing suitable contact metals.

The figure of merit of a PV cell is the power-conversion efficiency $\eta$, which can be expressed as

$$\eta = (I_m \cdot V_m)/P_{in} = (FF \cdot I_{SC} \cdot V_{OC})/P_{in} \quad (1)$$

where $I_m$ and $V_m$ are the output current and voltage, respectively, when the power generation ($=I_m \times V_m$) is at a maximum, $P_{in}$ is the incident power, and $FF$ is the fill factor indicating the power-delivery capability of a PV cell. The extraction of the key performance parameters is illustrated in Figure 4b. For our devices, $FF$ ranged from 0.42–0.56 under different illumination intensities. The $P_{in}$ is estimated by considering the total area of the SWNT sections perpendicular to the incident direction as the actual effective area of the SWNT PV cells, which was obtained by measuring the actual diameter and spanning length of each SWNT with atomic force microscopy (AFM) and SEM. Since SWNTs tend to form bundles, an average diameter of 5.2 nm for the SWNT bundles in the device was measured. The $P_{in}$ is estimated to be ≈33.4 nW for the SWNT PV cell with 146 SWNT bundles bridging the electrodes under an illumination intensity of 8.8 W cm$^{-2}$. Thus, a photoresponsitivity of $I_{SC}/P_{in} \approx 46.7$ mA W$^{-1}$ and an efficiency of $\eta \approx 0.80\%$ can be deduced. Similarly, the photoresponsitivity and efficiency are estimated to be 43.6 mA W$^{-1}$ and 0.69%, respectively, for the illumination intensity of 6.7 W cm$^{-2}$. Significantly, the obtained $\eta$ is remarkably high considering that the thin-monolayer SWNTs were used to construct the cells.

In the experiment, the dependency of the cell performance parameters on the incident power density ($P_0$) was studied. As shown in Figure 4c, both lg($I_{SC}$) and $V_{OC}$ increase logarithmically with $P_0$, and $FF$ increases from 0.42 to 0.56 with increased $P_0$ in the measure range. As a result, $\eta$ increases from ≈0.26% to ≈0.80% when the incident power increases from 64 mW cm$^{-2}$ to 8.8 W cm$^{-2}$. Therefore, the cell efficiency can be effectively enhanced by increasing the illumination power density. At $P_0 = 100$ mW cm$^{-2}$ (1 sun intensity), the cell shows a $\eta$ of ≈0.31%. Considering the actual effective area of the cell, the maximum $I_{SC}$ for the monolayer SWNT cell can be up to a high value of 405.7 mA cm$^{-2}$ when illuminated by the incident power of 8.8 W cm$^{-2}$, while the $I_{SC}$ for a commercially available planar monosilicon cell is only about 0.7 mA cm$^{-2}$.[35] Despite monolayer SWNTs applied as the photoactive region, the $I_{SC}$ obtained by our cell has shown great superiority compared to other high-performance SWNT-composite-based PV cells. The $I_{SC}$ differences between our device and these devices are 1.98 mA cm$^{-22}$ compared to 81 mA cm$^{-2}$ (under an illumination of 50 mW cm$^{-2}$),[36] 52.7 mA cm$^{-22}$ compared to 44.4 mA cm$^{-22}$ (under an illumination of 1.15 W cm$^{-22}$),[35] and 4.5 mA cm$^{-22}$ compared to 0.12 mA cm$^{-22}$ (under an illumination of 100 mW cm$^{-2}$).[37]

Since the SWNTs have only a thickness of 5.2 nm, only a small fraction of incident power can be absorbed by the device. Therefore, the $\eta$ based on the actual absorbed power should be much higher than the measured value. In order to evaluate the actual power-conversion efficiency, a high-frequency electromagnetic finite-element simulation is used to estimate the actual absorbed power by the SWNTs in the system (see Supplementary Information, particularly the discussion, Animation 1, and Animation 2). In the simulation, each SWNT bundle is modeled as a dielectric cylinder with a complex permittivity of $\varepsilon(\omega) = \varepsilon_r(\omega) + i\varepsilon_i(\omega)$ and the periodic boundary condition is utilized to account for the array structure. The role of the metal electrodes and substrate and the coupling between neighboring SWNT bundles are taken into account. Figure 5 shows the simulated optical-field distribution around the device (Figure 5a and b) and power-absorption spectra as a function of the photon energy (Figure 5c and d). The total absorbed incident power can be obtained by integrating the power-absorption spectrum weighted by the power density component of the used solar-simulated spectrum, which can be expressed as

$$P = \int \frac{dP_S}{d(\hbar\omega)} \times P_a(\hbar\omega) d(\hbar\omega) \quad (2)$$

where $\frac{dP_S}{d(\hbar\omega)}$ is the incident-power-density component distribution with the photon energy and $P_a(\hbar\omega)$ is the absorbed power per unit monochromatic incident power density. With the simulation, a total actual absorbed power of about 2.06 nW by SWNT bundles is estimated for the illumination intensity of 8.8 W cm$^{-2}$. Thus, a $\eta$ of 12.6% can be estimated correspondingly. Similarly, a total absorbed power of about 0.023 nW and a $\eta$ of 5.1% are estimated for the illumination intensity of 100 mW cm$^{-2}$. This $\eta$ for our devices is 51 times higher than that of the SWNT polymer, poly(3-octylthiophene) (P3OT), blend PV cells ($\eta \approx 0.1\%$[38] or 0.04%[39,40] under the illumination intensity of 100 mW cm$^{-2}$), in which SWNTs were employed as the electron acceptors.

For the obtainment of high $\eta$, a key factor can be attributed to the well-designed device structure, which causes the formation of a strong built-in electric field and a wide photoactive region in our device (spanning the whole SWNT between source and drain electrodes, while the photoactive region for the SWNT p–n junction is only near the narrow p–n junction[41]). On the other hand, another important reason is that the series resistance of PV cells, which arises primarily from the metal–nanotube contact resistance,[28] was significantly reduced by the ultrasonic nanowelding technique. Our previous studies have shown that ultrasonic nanowelding can decrease the contact resistance by three to four orders of magnitude.[23] A qualitative explanation for the effect of series resistance can be understood from the equivalent circuit of the SWNT PV cell shown in Figure 4d. According to Figure 4d, the actual short-circuit current in our devices should be expressed as

$$I_{SC} = I_{ph} - I_D = I_{ph} - I_S\left[\exp\left(\frac{q(I_{SC} \cdot R_S)}{nkT}\right) - 1\right] \quad (3)$$

where $I_{ph}$ is the photocurrent, $I_D$ is the forward biased current of the SWNT PV device, $I_S$ is the reverse saturation current, $R_S$ is the sum of the series resistance of the SWNT PV device (the effective total of the contact resistances and the nanotube

  

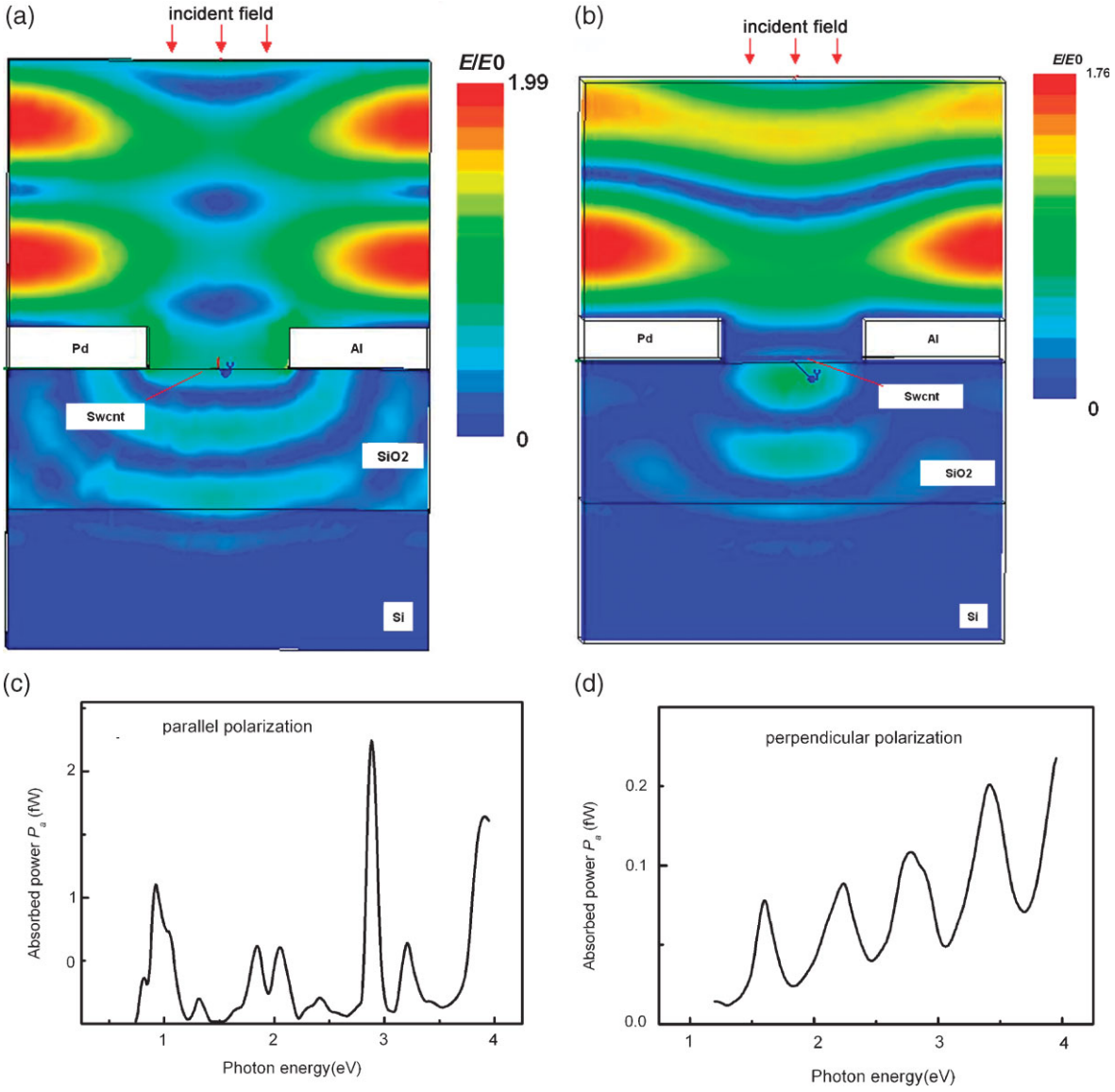


**Figure 5.** Optical-field distribution around the device and power-absorption spectra as a function of the photon energy obtained by the high-frequency electromagnetic finite-element simulation. a, b) The optical-field distribution under monochromatic illumination of 1.4 eV for the cases of the optical field parallel (a) and perpendicular (b) to the SWNT axis (parallel and perpendicular polarization). *E*0 is the amplitude of the incident optical field; the lattices in the scaleplates of (a) and (b) represent a gradient of $E/E0 \approx 0.124$ and $\approx 0.110$, respectively. c, d) The power-absorption spectra per SWNT bundle for the parallel (c) and perpendicular (d) polarization case. The absorbed power under different photon energy is normalized to unity monochromatic incident power density.

resistance), and $q$, $n$, $k$, and $T$ are the electron charge, ideality factor, Boltzmann's constant, and absolute temperature, respectively. In most traditional Si PV cells $R_S$ is small enough ($<1\ \Omega$) so that its effect is negligible, while in the SWNT PV cells $R_S$ is large and needs to be considered. If no further post treatment is done for the contacts, $R_S$ could reach up to tens of megaohms for individual SWNT diodes.[23] By fitting the dark $I$–$V$ curve of the device with the following diode equation,

$$I = I_S[\exp[q(V - IR_S)/nkT] - 1] \quad (4)$$

where $I$ and $V$ are the diode current and biasing voltage, respectively, we estimated a low series resistance of $R_S \approx 271\ \Omega$ for the nanowelded device. According to Equation (3), $I_{SC}$ is largely enhanced with a significant decrease of $R_S$. Thus, $\eta$ can be effectively improved.

In summary, a SWNT PV solar microcell based on nanowelded metal(A)/nanotube/metal(B) junctions has been demonstrated. The monolayer SWNT microcell showed a large open-circuit voltage of $V_{OC} \approx 0.31$ V and a power-conversion efficiency of $\eta \approx 0.80\%$ under solar-light illumination of 8.8 W cm$^{-2}$. It was found that the cell $\eta$ can be effectively enhanced with the increase of the illumination power density. By simulating the actual absorbed incident power, a high actual $\eta$ of 12.6% and 5.1% was estimated for the solar illumination density of 8.8 W cm$^{-2}$ and 100 mW cm$^{-2}$, respectively. The high $\eta$ is attributed to the combination of the favorable device structure design and the significantly

  

decreased series resistance achieved by the ultrasonic nanowelding technique. Further improvements in $\eta$ can be expected by choosing SWNTs with a more suitable bandgap,[1] adopting the multilayered different diameters of SWNT arrays, and further decreasing the channel length and the series resistance of the cells. Our results demonstrate the vast potential of SWNTs for PV applications.

### Experimental Section

*Alignment of SWNTs with AC dielectrophoresis method:* Firstly, a high-frequency AC bias with a frequency of 5 MHz and a peak-to-peak voltage of 10 V was applied to the source and drain electrodes. Then, a drop of SWNT suspension with a concentration of $\approx$0.5 $\mu$g mL$^{-1}$ was introduced onto the structured wafer. Thus, the dielectrophoretic force, produced by the interaction of the nonuniform electric field with the electric-field-induced dipole in SWNTs, propelled the SWNTs toward the location with the highest electric-field strength and align directionally between the source and drain electrodes.[22,42] In the alignment process, the wafer was kept at 55 °C in order to enhance the evaporation speed of the 1,2-dichloroethane solvent. The AC bias was switched off after the solvent completely evaporated.

*Ultrasonic nanowelding of SWNTs to metal electrodes:* An $Al_2O_3$ crystal with a 56.4-$\mu$m-diameter circular pressure surface and a root-mean-square roughness of 0.2 nm was used as the welding head to bond the SWNTs and metal electrodes. A force of 4.9 mN was applied to the welding head to press SWNTs against the metal electrodes. At the same time, the welding head vibrated at an ultrasonic frequency of 60 KHz and output an ultrasonic power of 10 mW. The nanowelding process lasted 10 ms under room temperature. Thus, the two ends of SWNTs could be embedded and welded into the electrodes under the combined effect of the ultrasonic and clamping force.

**Keywords:**
carbon nanotubes · photovoltaic cells · power conversion efficiency · schottky barriers

[1] M. A. Green, in *Solar Cells: Operating Principles, Technology, and Applications*, Prentice–Hall, Englewood Cliffs, NJ **1982.**
[2] G. Yu, J. Gao, J. Hummelen, F. Wudl, A. J. Heeger, *Science* **1995**, *270*, 1789.
[3] S. G. Bailey, S. L. Castro, R. P. Raffaelle, S. Fahey, T. Gennett, P. Tin, *IEEE Proceedings of 3rd World Conference on Photovoltaic Energy Conversion* **2003**, *3*, 2690.
[4] R. Saito, G. Dresselhaus, M. S. Dresselhaus, in *Physical Properties of Carbon Nanotubes*, Imperial College, London **1998.**
[5] M. J. O'Connell, S. M. Bachilo, C. B. Huffman, V. C. Moore, M. S. Strano, E. H. Haroz, K. L. Rialon, P. J. Boul, W. H. Noon, C. Kittrell, J. Ma, R. H. Hauge, R. B. Weisman, R. E. Smalley, *Science* **2002**, *297*, 593.
[6] A. Hagen, T. Hertel, *Nano Lett.* **2003**, *3*, 383.
[7] J. Ando, *J. Phys. Soc. Jpn.* **1997**, *66*, 1066.
[8] T. G. Pedersen, *Phys. Rev. B* **2003**, *67*, 073401.
[9] J. W. G. Wilder, L. C. Venema, A. G. Rinzler, R. E. Smalley, C. Dekker, *Nature* **1998**, *391*, 59.
[10] T. W. O. Odom, J. L. Huang, P. Kim, C. M. Lieber, *Nature* **1998**, *391*, 62.
[11] Y. Zhang, S. Iijima, *Phys. Rev. Lett.* **1999**, *82*, 3472.
[12] M. Freitag, Y. Martin, J. A. Misewich, R. Martel, P. Avouris, *Nano Lett.* **2003**, *3*, 1067.
[13] A. Fujiwara, Y. Matsuoka, H. Suematsu, N. Ogawa, K. Miyano, H. Kataura, Y. Maniwa, S. Suzuki, Y. Achiba, *Jpn. J. Appl. Phys.* **2001**, *40*, L1229.
[14] C. D. Spataru, S. Ismail-Beigi, L. X. Benedict, S. G. Louie, *Phys. Rev. Lett.* **2004**, *92*, 017403.
[15] J. U. Lee, *Appl. Phys. Lett.* **2005**, *87*, 073101.
[16] M. S. Fuhrer, B. M. Kim, T. Du1rkop, T. Brintlinger, *Nano Lett.* **2002**, *2*, 755.
[17] M. Freitag, V. Perebeinos, J. Chen, A. Stein, J. C. Tsang, J. A. Misewich, R. Martel, P. Avouris, *Nano Lett.* **2004**, *4*, 1063.
[18] J. Guo, C. Yang, Z. M. Li, M. Bai, H. J. Liu, G. D. Li, E. G. Wang, C. T. Chan, Z. K. Tang, W. K. Ge, X. D. Xiao, *Phys. Rev. Lett.* **2004**, *93*, 017402.
[19] S. Barazzouk, S. Hotchandani, K. Vinodgopal, P. V. Kamat, *J. Phys. Chem. B* **2004**, *108*, 17015.
[20] A. Javey, Q. Wang, W. Kim, H. Dai, *Proceeding IEDM* **2003**, 741.
[21] S. J. Tans, A. R. M. Verschueren, C. Dekker, *Nature* **1998**, *393*, 49.
[22] C. X. Chen, Y. F. Zhang, *J. Phys. D: Appl. Phys.* **2006**, *39*, 172.
[23] C. X. Chen, L. J. Yan, E. S. W. Kong, Y. F. Zhang, *Nanotechnology* **2006**, *17*, 2192.
[24] C. X. Chen, D. Xu, E. S. W. Kong, Y. F. Zhang, *IEEE Electron Device Lett.* **2006**, *27*, 852.
[25] P. G. Collins, M. S. Arnold, P. Avouris, *Science* **2001**, *292*, 706.
[26] R. J. Chen, N. R. Franklin, J. Kong, J. Cao, T. W. Tombler, Y. Zhang, H. Dai, *Appl. Phys. Lett.* **2001**, *79*, 2258.
[27] M. Shim, G. P. Siddons, *Appl. Phys. Lett.* **2003**, *83*, 3564.
[28] H. M. Manohara, E. W. Wong, E. Schlecht, B. D. Hunt, P. H. Siegel, *Nano Lett.* **2005**, *5*, 1469.
[29] S. Heinze, J. Tersoff, R. Martel, V. Derycke, J. Appenzeller, P. Avouris, *Phys. Rev. Lett.* **2002**, *89*, 106801.
[30] V. Derycke, R. Martel, J. Appenzeller, P. Avouris, *Appl. Phys. Lett.* **2002**, *80*, 2773.
[31] A. Javey, J. Guo, Q. Wang, M. Lundstrom, H. Dai, *Nature* **2003**, *424*, 654.
[32] N. Neophytou, J. Guo, M. Lundstrom, *IEEE Trans. Nanotechnology* **2006**, *5*, 385.
[33] F. Léonard, J. Tersoff, *Phys. Rev. Lett.* **1999**, *83*, 5174.
[34] J. Nelson, in *The Physics of Solar Cells*, Imperial College, London **2003.**
[35] R. E. Camacho, A. R. Morgan, M. C. Flores, T. A. McLeod, V. S. Kumsomboone, B. J. Mordecai, R. Bhattacharjea, W. Tong, B. K. Wagner, J. D. Flicker, S. P. Turano, W. J. Ready, *JOM* **2007**, *59*, 39.
[36] A. Kongkanand, R. M. Dom'nguez, P. V. Kamat, *Nano Lett.* **2007**, *7*, 676.
[37] B. J. Landi1, R. P. Raffaelle1, S. L. Castro, S. G. Bailey, *Prog. Photovolt: Res. Appl.* **2005**, *13*, 165.
[38] E. Kymakis, G. A. J. Amaratunga, *Rev. Adv. Mater. Sci.* **2005**, *10*, 300.
[39] E. Kymakis, G. A. J. Amaratunga, *Appl. Phys. Lett.* **2002**, *80*, 112.
[40] S. Bhattacharyya, E. Kymakis, G. A. J. Amaratunga, *Chem. Mater.* **2004**, *16*, 4819.
[41] D. A. Stewart, F. Léonard, *Nano Lett.* **2005**, *5*, 219.
[42] J. Q. Li, Q. Zhang, N. Peng, Q. Zhu, *Appl. Phys. Lett.* **2005**, *86*, 153116.

Received: December 25, 2007
Published online: August 14, 2008

  